Monthly Notices of the ROYAL ASTRONOMICAL SOCIETY

MNRAS **518,** 3593–3605 (2023) https://doi.org/10.1093/mnras/stac3221
Advance Access publication 2022 November 9

An accurate set of $H_3O^+ - H_2$ collisional rate coefficients for non-LTE modelling of warm interstellar clouds

Sándor Demes [1★] François Lique,[1★] Alexandre Faure [2★] and Floris F. S. van der Tak[3]

[1] *Univ Rennes, CNRS, IPR (Institut de Physique de Rennes) - UMR 6251, F-35000 Rennes, France*
[2] *IPAG, Université Grenoble Alpes & CNRS, CS 40700, F-38058 Grenoble, France*
[3] *SRON Netherlands Institute for Space Research & Kapteyn Astronomical Institute, University of Groningen, 9747 AD Groningen, the Netherlands*

Accepted 2022 November 3. Received 2022 November 3; in original form 2022 October 18

ABSTRACT

Hydronium (H_3O^+) was first detected in 1986 in interstellar molecular clouds. It was reported in many Galactic diffuse and dense regions, as well as in extragalactic sources. H_3O^+ plays a major role both in interstellar oxygen and water chemistry. However, despite the large number of H_3O^+ observations, its collisional excitation was investigated only partially. In this work, we study the state-to-state rotational (de-)excitation of *ortho*- and *para*-H_3O^+ in collisions both with *ortho*- and *para*-H_2. The cross sections are calculated within the close-coupling formalism using a highly accurate potential energy surface developed for this system. The rate coefficients are computed up to a kinetic temperature of 300 K. Transitions between the lowest 21 rotation-inversion states were studied for *para*-H_3O^+, and the lowest 11 states for *ortho*-H_3O^+, i.e. all levels with rotational energies below 430 K ($\sim$300 cm^{-1}) are considered. In order to estimate the impact of the new rate coefficients on the astrophysical models for H_3O^+, radiative transfer calculations were also carried out. We have examined how the new collisional data affect the line intensities with respect to older data previously used for the interpretation of observations. By analysing all detected transitions we find that our new, accurate rate coefficients have a significant impact (typically within a factor of 2) on radiation temperatures, allowing more accurate estimation of column densities and relative abundances of hydronium, especially in warm molecular clouds, paving the path towards better interpretation of interstellar water and oxygen chemistry.

Key words: astrochemistry – molecular data – molecular processes – radiative transfer – methods: laboratory: molecular – ISM: molecules.

1 INTRODUCTION

The presence of the hydronium cation (H_3O^+) in various interstellar molecular clouds was reported by many observational research papers, including its prediction in a fundamental work by Herbst & Klemperer (1973) followed by the first nearly simultaneous observations in 1986 by Wootten et al. (1986) and Hollis et al. (1986), then the confirming detections in the 90s of the past century (Wootten et al. 1991; Phillips, van Dishoeck & Keene 1992; Timmermann et al. 1996), and later in early 2000s by van der Tak et al. (2006), van der Tak, Aalto & Meijerink (2008). In the 2010s, there were several new observations of H_3O^+ reported in different interstellar environments (Benz et al. 2010; Gerin et al. 2010; González-Alfonso et al. 2013; Lis et al. 2014; Indriolo et al. 2015; Benz et al. 2016; Ando et al. 2017), while the most recent studies were published by Martín et al. (2021) and Holdship et al. (2022). The existing observational detections of hydronium will be reviewed thoroughly in Section 2. Chemical models involving hydronium were also developed intensively, as one can see, for example, in the works of Sternberg & Dalgarno (1995), Goicoechea & Cernicharo (2001), Hollenbach et al. (2012), van Dishoeck, Herbst & Neufeld (2013), Faure et al. (2019), which all reported that it plays a key role in oxygen and water chemistry of the interstellar medium (ISM) nominating it as a crucial chemical species in interstellar ion-molecule reaction schemes. The relative abundances of H_3O^+ and H_2O may be also used to measure the ionization rates of molecular clouds both in the Milky Way (van der Tak et al. 2006) as well as in external galaxies (van der Tak et al. 2008, 2016). According to Phillips et al. (1992), measuring the abundance of the H_3O^+ cation can indirectly provide the abundance of interstellar water. To quantitatively determine its role in different astrophysical environments, however, the details of both its radiative and collisional excitation should be taken into account in addition to its formation and destruction paths.

The formation mechanisms of H_3O^+ in molecular clouds as well as its dissociative recombination pathways were briefly summarized in our previous paper (Demes et al. (2021), referred as Paper II hereinafter). The relevant details about the chemistry of hydronium are discussed by van Dishoeck et al. (2013) and Hollenbach et al. (2012), while its dissociative recombination is carefully studied by Jensen et al. (2000). The high-resolution spectroscopy measurements for H_3O^+ are collected and analysed by Yu et al. (2009). While the spectroscopy of the pure rotational levels of hydronium is rather complete, its hyperfine structure remains unresolved (Yu et al. 2009). For molecules with non-zero nuclear spin, hyperfine splitting is usually only observable if they contain a nucleus with spin $I \geq 1$, such as ^{17}O or D (van der Tak et al. 2009). In interstellar clouds, such splitting may be observed for the H_3O^+ isotopologues $H_3{}^{17}O^+$ and H_2DO^+. Its electron-impact excitation was studied also

★ E-mail: sandor.demes@univ-rennes1.fr (SD); francois.lique@univ-rennes1.fr (FL); alexandre.faure@univ-grenoble-alpes.fr (AF)

earlier (Faure & Tennyson 2003). The collisional excitation studies of hydronium are very limited however. The first, approximated collisional cross section were provided by Offer & van Hemert (1992), which has given a basis then for interpreting the observations of H_3O^+ in both dense and diffuse interstellar clouds. However, the authors did not report rate coefficients, so their data were scaled in combination with NH_3 collisional data of Danby et al. (1988). Later El Hanini et al. (2019) studied the rotational excitation of hydronium by helium atoms (as a template for H_2), but for a limited energy and temperature range (up to 50 K). Recently we have computed state-to-state collisional rate coefficients up to 100 K for the rotational excitation of both *ortho*- and *para*-H_3O^+ in collision with *para*-H_2 (Paper II). A detailed discussion about the previous collisional excitation studies (Offer & van Hemert 1992; El Hanini et al. 2019) was already given in this work, including a comparative analysis of the cross sections and rate coefficients.

It is worth to emphasize again that, according to the authors of several observational studies [see, for example, the works by Wootten et al. (1991), van der Tak et al. (2008)] reliable and precise collisional rate coefficients are needed to correctly interpret the astrophysical observations of H_3O^+ in interstellar clouds. Without such data the molecular abundances could be only approximated, assuming local thermodynamic equilibrium (LTE), which is usually not a good approximation for typical interstellar conditions (Roueff & Lique 2013).

In this work, we provide a complete set of rotational excitation cross sections and thermal rate coefficients for the $H_3O^+ - H_2$ collisional system, which are calculated based on an accurate 5-dimensional interaction potential (Demes et al. (2020), referred as Paper I hereinafter). The new collisional data presented here have several crucial improvements compared to Paper II: the calculations are extended to *ortho*-H_2, and we compute accurate rate coefficients up to 300 K (over 100 K in Paper II). To demonstrate the impact of the new collisional data, radiative transfer calculations are provided as well and their results obtained with different sets of rate coefficients are compared.

The paper is organized as follows: In Section 2, the literature of the H_3O^+ observations is reviewed in a chronological order. In Section 3, the details of the interaction potential as well as the scattering calculations are presented. The state-to-state collisional data for the rotational de-excitation of H_3O^+ by H_2 are discussed in Section 4, where Section 4.1 introduces the cross sections and Section 4.2 presents the thermal rate coefficients, respectively. In Section 5, we also report radiative transfer calculation results, while our concluding remarks are drawn in Section 6.

2 OBSERVATIONAL DETECTIONS OF H_3O^+

The first prediction of the presence of H_3O^+ in dense molecular clouds of the Orion/KL and Sgr B2 regions (where the approximate hydrogen density is $\sim 10^6\,\mathrm{cm}^{-3}$) was given by Herbst & Klemperer (1973). More than a decade later Wootten et al. (1986) and Hollis et al. (1986) almost simultaneously reported the first detections. Both groups used the NRAO 12 m telescope and both measured the 307.2 GHz emission line in the OMC-1 and Sgr B2 sources. The confirming detection was reported soon by Wootten et al. (1991) in the same environments with the identification of the $3_2^+ \rightarrow 2_2^-$ transition of *ortho*-H_3O^+ at 364 GHz (note that the rotational states of H_3O^+ are denoted by j_k^ϵ, where j is the total angular momentum, k is its projection on the C_3 main rotational axis, and $\epsilon = \pm$ is the inversion symmetry index, see Rist, Alexander & Valiron (1993) for more details). In these first observations the authors reported kinetic temperatures above 70 K with an H_2 density of about $10^6\,\mathrm{cm}^{-3}$, and they also emphasize the importance of a non-local thermodynamic equilibrium (non-LTE) analysis, since the low excitation temperature of H_3O^+ are poorly described in an LTE approach (which was the only available model for H_3O^+ at that time due to the lack of collisional data). Later Phillips et al. (1992) reported a more clear detection of three – 396, 364, and 307 GHz – submillimeter lines in more than 10 Galactic sources, besides the spectroscopically confusing OMC-1 and Sgr B2 clouds, the G34.3 + 0.15 and W51 clouds as well as different high-mass star formation regions, for example the W3 IRS 5 cloud. Most of them are exhibiting high-density ($n_{H_2} \approx 10^6 - 10^7\ \mathrm{cm}^{-3}$) and high-temperature ($T_{\mathrm{kin}} \gtrsim 50$ K) conditions. The authors found that the typical H_3O^+ abundance is 10^{-10} – 10^{-9} in these regions. The $4_3^- \rightarrow 3_3^+$ far-infrared emission line of H_3O^+ at 69.524 μm (4312 GHz) was measured soon after by Timmermann et al. (1996) in the Orion BN-IRc2 region with NASA's Kuiper Airborne Observatory. The authors reported it as a possible H_3O^+ detection, which might originate from very dense clumps. They also reported high hydrogen densities ($\gtrsim 5 \times 10^8\ \mathrm{cm}^{-3}$) and temperatures ($\gtrsim 100$ K) in this environment. For their model and analysis the authors used scaled, approximated collisional rate coefficients based on the work of Offer & van Hemert (1992), and they estimated the column densities of H_3O^+ in the range from $9 \times 10^{13}\,\mathrm{cm}^{-2}$ (under LTE conditions and 300 K) up to $7 \times 10^{16}\ \mathrm{cm}^{-2}$ (under non-LTE conditions and $T = 100$ K).

Ten years later van der Tak et al. (2006) detected strong emission in the H_3O^+ 364 GHz and 307 GHz lines both in the M core and OH envelope of the Sgr B2 region with the APEX telescope. The authors reported column densities in the range between 3.7×10^{15} and $1.36 \times 10^{16}\,\mathrm{cm}^{-2}$ in the envelope and in the core, respectively, and they found the hydronium abundance to be $\sim 3 \times 10^{-9}$ relative to H_2 and the H_3O^+/H_2O ratio to be about 1/50 in this region. The physical conditions in the M core are $T = 200$ K and $n_{H_2} = 10^7\,\mathrm{cm}^{-3}$, while in the low-density OH envelope the temperature is about 60 K only and the H_2 density is $10^6\ \mathrm{cm}^{-3}$. Later hydronium was detected in extra-galactic environments as well by van der Tak et al. (2008). Observations with the JCMT targeted the well-known 364 GHz emission line of the $3_2^+ \rightarrow 2_2^-$ transition in the centres of M 82 and Arp 220, where the expected kinetic temperature is $\sim$100 K and the hydrogen density is at least $10^5\,\mathrm{cm}^{-3}$. With an estimated *para*-H_3O^+ column density of $(0.7 - 1.3) \times 10^{13}\ \mathrm{cm}^{-2}$ for Arp 220 and $(3.0 - 5.5) \times 10^{13}\,\mathrm{cm}^{-2}$ for M 82, the authors found that the typical hydronium abundance is $(2 - 10) \times 10^{-9}$ relative to H_2. For radiative transfer modelling of these environments both in the work of van der Tak et al. (2006) and van der Tak et al. (2008) the scaled collisional data were derived from Offer & van Hemert (1992) and Danby et al. (1988).

The W3 IRS 5 cloud was later studied by Benz et al. (2010), searching for the major hydrides in this region of the ISM. The authors detected several rotational transitions of H_3O^+ in this high-mass star-forming region using HIFI on the *Herschel Space Observatory*. Emissions from the $4_3^+ \rightarrow 3_3^-$ (1031.3 GHz), $4_2^- \rightarrow 3_2^+$ (1069.8 GHz), $6_2^+ \rightarrow 6_2^-$ (1454.6 GHz), and $2_1^+ \rightarrow 2_1^-$ (1632.1 GHz) *ortho*- and *para*-H_3O^+ transitions were measured. The authors found the column density is typically about $10^{14}\,\mathrm{cm}^{-2}$, and the corresponding hydronium abundance is $4.2(\pm\ 1) \times 10^{-10}$ relative to atomic hydrogen. The gas density of the environment exceeds $10^7\,\mathrm{cm}^{-3}$, and the rotational temperature is about 205 – 285 K (the gas temperature can be even higher). In parallel a weak 984 GHz absorption line of H_3O^+ was also detected with the HIFI/*Herschel* along the massive star-forming region G10.6-0.4 (W31C) (Gerin et al. 2010). The authors derived a hydronium column density $N(H_3O^+) \sim 4 \times 10^{13}\,\mathrm{cm}^{-2}$ for the V_{LSR} velocity range of 7 – 45 km s $^{-1}$. According to Gerin et al. (2010) in this diffuse cloud the hydrogen density is only about 10^2 – $10^3\,\mathrm{cm}^{-3}$ and the temperature can be as low as 5 K.

González-Alfonso et al. (2013) also reported excited hydronium in the extragalactic NGC 4418 and Arp 220 regions based on *Herschel*/PACS observations. The column density of H_3O^+ is found to be about $(0.9-2.7)\times 10^{16}$ cm^{-2} in Arp 220, and the observed pure inversion, metastable lines have a very high rotational temperature of ∼500 K. The authors characterize the source as a relatively low density ($\gtrsim 10^4$ cm^{-3}) interclump medium. They presented the detection of a series of lines of hydronium in the 70 – 180 μm spectral range, involving several states with $j = 2-5$ rotational quantum numbers and above. It is also shown by González-Alfonso et al. (2013) that the states with $K > 1$ projection quantum numbers can be populated only through collisions or via molecular formation in high-lying levels. The authors still used scaled rate coefficients based on the data from Offer & van Hemert (1992) and Danby et al. (1988) for non-LTE modelling of the H_3O^+ excitation. In the NGC 4418 source the work reports $(5-8)\times 10^{15}$ cm^{-2} column densities and $T\sim 150$ K gas temperatures for the transitions from lower K (≤ 5) as well as $T\sim 500$ K for the ones from higher rotational states. Just a year later, Lis et al. (2014) presented the results of *Herschel* observations of the $6_6^- \rightarrow 6_6^+$ and $9_9^- \rightarrow 9_9^+$ inversion transitions of hot hydronium toward the diffuse Sagittarius B2(N) and W31C sources, with estimated column densities of 7×10^{14} cm^{-2} and 1.2×10^{13} cm^{-2}, respectively. The authors report rotational temperatures of about 500 K and 380 K, so the kinetic temperature can reach 400–600 K. The next *Herschel* observation of H_3O^+ was presented by Indriolo et al. (2015) for diffuse interstellar clouds along 20 Galactic sight lines toward bright submillimeter continuum sources. The authors measured the $1_1^- \rightarrow 1_1^+$ (1655.8 GHz) transition in absorption and the $0_0^- \rightarrow 1_0^+$ (984.7 GHz) line in emission and they derived column densities in the range from 3×10^{14} up to 1.66×10^{13} cm^{-2} depending on the source. The authors suggested a kinetic temperature of 100 K, which represents the average temperature in diffuse clouds, and they considered hydrogen densities as low as 35 cm^{-3}. Another observation by *Herschel* (Benz et al. 2016) reported the $4_3^+ \rightarrow 3_3^-$ (1031.3 GHz) emission line of *ortho*-H_3O^+ in several young stellar objects. The authors considered a wide range of gas densities (10^4 – 10^6 cm^{-3}) and kinetic temperatures (from 10 K up to several hundreds of K).

Emission from the $3_2^+ \rightarrow 2_2^-$ line of H_3O^+ (364 GHz) was detected again recently by Ando et al. (2017) in the starburst galaxy NGC 253, based on ALMA Band 7 observations. According to the authors, this is a dense ($n_{H_2} \geq 10^6$ cm^{-3}) and hot environment with typical kinetic temperatures ≥100 K. The latest observations of hydronium were reported by Holdship et al. (2022) within the ALMA Comprehensive High-Resolution Extragalactic Molecular Inventory. The research has targeted the central molecular zone of the extragalactic NGC 253 source, studying the impact of cosmic-ray ionization rates on the abundance ratio of H_3O^+ and SO. The authors estimated the fractional abundance of hydronium to be about 5×10^{-10} – 10^{-9}. They varied the gas density and temperature in a wide range, respectively from 10^4 to 10^7 cm^{-3} and from 50 up to 300 K. Their analysis was performed based on the well-studied 364 GHz ($3_2^+ \rightarrow 2_2^-$) and 307 GHz ($1_1^+ \rightarrow 2_1^+$) transitions of H_3O^+, leading to a conclusion that the H_2 density most likely vary between $(0.4-9.8)\times 10^5$ cm^{-3}, depending on the source.

3 METHODS

In Paper II, we described the relevant approach of the scattering calculations. Here we briefly summarize the most important points and provide the details for the new calculations that are presented in this paper.

3.1 Potential energy surface

The scattering calculations were performed using our recent 5D rigid-rotor potential energy surface (PES) for the $H_3O^+ - H_2$ interaction (Paper I). This potential was calculated by the rigorously tested and very accurate CCSD(T)-F12 (explicitly correlated coupled-cluster theory with singles and doubles with perturbative corrections for triple excitations) *ab initio* theory with a moderate-size aug-cc-pVTZ (augmented correlation-consistent polarised valence-triple-ζ) basis set. This combination of 'method + basis set' ensures the necessary high quality of the PES with a reasonable computational cost.

The collisional system is defined in a Jacobi coordinate system using the molecular frame (body-fixed) representation. Consequently, the centre of the coordinate system is set in the centre of mass (c.o.m.) of the target H_3O^+ cation. One spatial parameter (R) defines the distance between the colliders, while four spherical angles describe the position and relative orientation of the H_2 projectile with respect to the origin of the coordinate system. The H_2 bond length was set at $r_{H\text{-}H} = 1.44874\,a_0$ (Bubin & Adamowicz 2003), and for H_3O^+ we used the experimental bond properties by Tang & Oka (1999): $r_{O\text{-}H} = 1.8406\,a_0$ and $\alpha_{H\text{-}O\,-\,H} = 113.6^\circ$.

The *ab initio* PES was fitted using a standard least square procedure, resulting in a set of 208 radial expansion functions for each R, with anisotropies up to $l_1 = 16$ and $l_2 = 4$. The root mean square (rms) residual was found to be lower than 1 cm^{-1} in the long-range of the potential and also in the well region (which is about 1887.2 cm^{-1} deep). The rms error on the expansion coefficients was also found to be smaller than 1 cm^{-1} in these regions of the PES. A cubic spline interpolation of the analytical coefficients was performed for distances between $R = 4-30\,a_0$, and it was smoothly connected then to standard extrapolations using the switch function proposed by Valiron et al. (2008). Since there are no experimental observables for the $H_3O^+ - H_2$ system, we cannot assess the accuracy of our interaction potential. However, from similar PES calculations by Faure, Lique & Wiesenfeld (2016), Pirlot et al. (2021), Godard Palluet, Thibault & Lique (2022), where the accuracy of the potential was estimated based on a comparison with experimental dissociation and/or bound states energies, we expect that its overall accuracy is at the wavenumber level of accuracy and is always better than 10 per cents. For full details about the interaction potential and the analytical fit, see Paper I.

We used the following units throughout this paper (until otherwise noted): atomic units (a_0) for distances ($1\,a_0 = 1$ bohr ≈ 5.29177×10^{-9} cm), wavenumbers (cm^{-1}) for energies (1 cm^{-1} ≈ 1.4388 K).

3.2 Scattering calculations

We have calculated the state-to-state rotational (de-)excitation cross sections and thermal rate coefficients for the collision of *ortho*- and *para*-H_3O^+ with *para*-H_2 in our previous work (Demes et al. 2021). This work is an extension of the previous one with several crucial improvements. First, we have studied all the possible nuclear spin isomers, so the calculations are extended to collisions with *ortho*-H_2 as well, which is the dominant collider in interstellar clouds with temperatures above 100 K. Second, we have significantly increased the interval of collision energies for the cross section calculations, which allowed us to compute accurate rate coefficients up to 300 K. These improved collisional data allow one to provide a precise non-LTE modelling for warm molecular clouds involving H_3O^+ (see, for example, the observations by van der Tak et al. (2008) at several hundred Kelvins).

In current work, we determined the cross sections by the full quantum (close-coupling, CC) approach using the HIBRIDON scattering code (Manolopoulos 1986; Alexander & Manolopoulos 1987). They were computed up to 1700 cm^{-1} total energies for H_3O^+ collisions with *ortho*(o)-H_2 and up to 1500 cm^{-1} total energies for collisions with *para*(p)-H_2. The o-H_3O^+ spin species is characterized with $k = 3n$ quantum numbers (where n are integer numbers), while all other k quantum numbers refer to p-H_3O^+.

We computed all inelastic cross sections for the transitions between rotational levels with an internal energy of $\leq$430 K ($\sim$300 cm^{-1}), including states up to 5_2^+ for p-H_3O^+ and 5_3^+ for o-H_3O^+. For the full list of the rotational states involved for H_3O^+, see Table A1 in Appendix A. Both the rotational basis (j_{max}) and the maximum total angular momentum (J_{tot}) were selected depending on the nuclear spin symmetry and collision energy. Their particular values are set based on preliminary convergence test calculations with the following convergence-threshold criteria: maximum 1 per cent mean deviation for j_{max} and 0.01 per cent mean deviation for J_{tot}. As discussed in Paper II, in order to adequately describe the strong resonances in the cross sections, a very small step size ($E_{step} = 0.1\,cm^{-1}$) was chosen at low collision energies, which was gradually increased then. The values of the j_{max}, J_{tot}, and E_{step} parameters, which were used in the calculations for the particular total energy intervals from E_{init} to E_{fin} are listed in Tables B1 and B2 of Appendix B. The values of j_{max} here refer to the highest rotational states of the H_3O^+ cation used in the CC calculations. For the H_2 projectile the two lowest rotational states were considered in the scattering calculations, i.e. $j_{H_2} = 0, 2$ for p-H_2 and $j_{H_2} = 1, 3$ for o-H_2. The convergence test calculations have shown that the $j_{H_2} = 2$ and 3 excited states of H_2 have a significant effect on the cross sections' magnitude and should not be neglected in the CC calculations. For a few energies we performed scattering calculations with a larger H_2 rotational basis as well ($j_{H_2} = 0 - 5$). We found that the impact from these additional hydrogen levels is usually not too large, they have a $\sim$ 5 per cent effect on the magnitude of the cross sections in general, which decreases with increasing collision energy. The largest relative difference detected in the collisional data calculated with this extended basis compared to what was computed in the systematic CC calculations is $\sim$ 25 per cent. Even the $j_{H_2} = 0 - 3$ basis is very large however, which makes the systematic quantum calculations extremely demanding computationally, especially in the case of the p-H_3O^+ target molecule, which is characterized with two times more levels than o-H_3O^+ when the same internal energy is considered. Thus, for example, for the p-H_3O^+ – o-H_2 collision in the high energy regime ($\geq$1450 cm^{-1}) the number of coupled channels exceeded 8000, for which the computational cost to calculate the cross sections for a defined total energy reaches several thousands of CPU-hours. According to our estimations, about 600.000 CPU-hours were spent in total for the calculation of all H_3O^+ – H_2 cross sections.

The rate coefficients were computed up to 300 K kinetic temperatures following the well-known integration method over a Maxwell–Boltzmann distribution of relative velocities:

$$k_{i\to f}(T) = \left(\frac{8}{\pi\mu k_B^3 T^3}\right)^{\frac{1}{2}} \int_0^\infty \sigma_{i\to f} E_c e^{-\frac{E_c}{k_B T}} dE_c, \quad (1)$$

where E_c is the collision or kinetic energy, $\sigma_{i\to f}$ is the energy-dependent cross section for the transition from a particular initial (i) to a final state (f), μ is the reduced mass of the collisional system and k_B is the Boltzmann constant in atomic units. By summing all possible error contributions (induced both in the PES and scattering calculations), we expect that the accuracy of the collisional rate coefficients is generally as low as a few per cents and always better than 25 – 30 per cent.

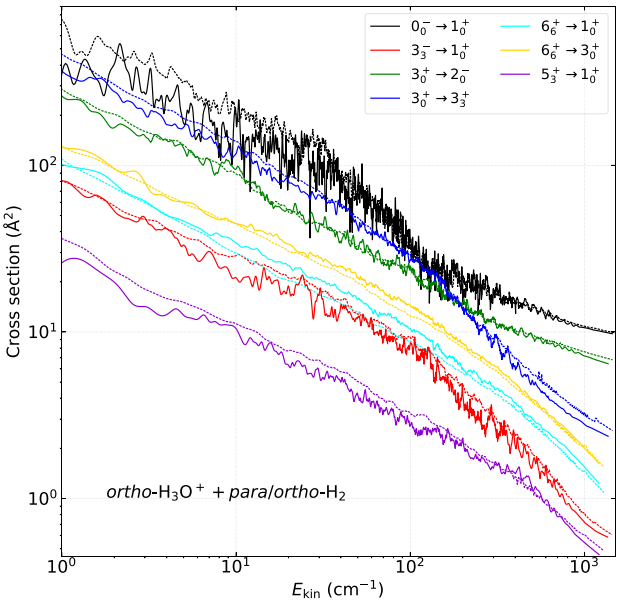

Figure 1. The variation of rotational de-excitation cross sections for some selected transitions of o-H_3O^+ in collision with p-H_2 (solid lines) and o-H_2 (dashed lines) projectiles.

4 RESULTS AND DISCUSSION

In Paper II, we have shown the behaviour of the $H_3O^+ - p$-H_2 rotational de-excitation cross sections and thermal rate coefficients over a limited energy and temperature range. We have presented a comparison of our state-to-state collisional data with the most relevant theoretical works for the $H_3O^+ - He$ (El Hanini et al. 2019) and for the $NH_3 - H_2$[1] (Bouhafs et al. 2017) collisions. We examined several Δj and Δk transitions in Paper II, showing that there is a significant difference between the cross sections we calculated and those of El Hanini et al. (2019) and Bouhafs et al. (2017) in the whole energy range considered (typically our cross sections are about an order of magnitude larger than those from the literature). Another important finding of Paper II is that there is no direct (linear) scaling between the compared quantities, so the new cross sections and rate coefficients have a significant importance, since they show a large improvement in quality in contrast with the previously published collisional data. Since such a comparative analysis with the available literature was provided and discussed in detail in our previous work, we are not repeating it here.

4.1 Rotational de-excitation cross sections

In Figs 1 and 2, the dependence of the H_3O^+ rotational de-excitation cross sections is presented with respect to the collision (kinetic) energy in collisions with both p-H_2 (solid lines) and o-H_2 (dashed lines). In Fig. 1 we compare the cross sections for o-H_3O^+ target

[1]Our motivation for the comparison with ammonia collisional data is related to their isoelectronic nature and structural similarities, and NH_3 was assumed to be a template for collisions with H_3O^+ for a long time.

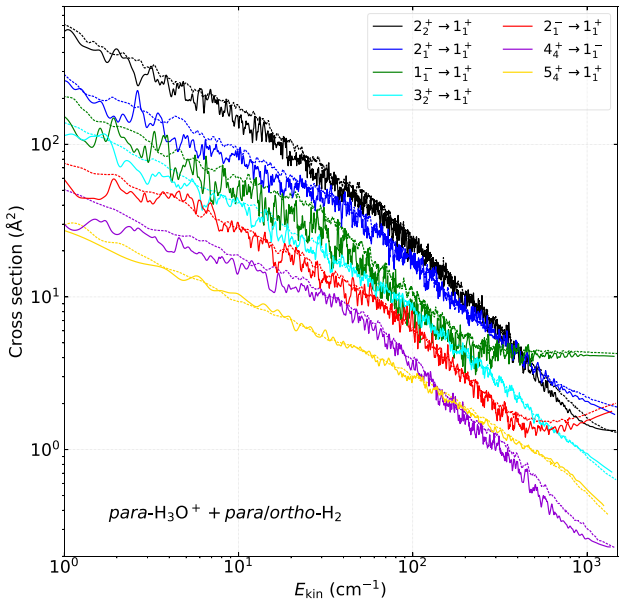

Figure 2. The variation of rotational de-excitation cross sections for some selected transitions of *p*-H_3O^+ in collision with *p*-H_2 (solid lines) and *o*-H_2 (dashed lines) projectiles.

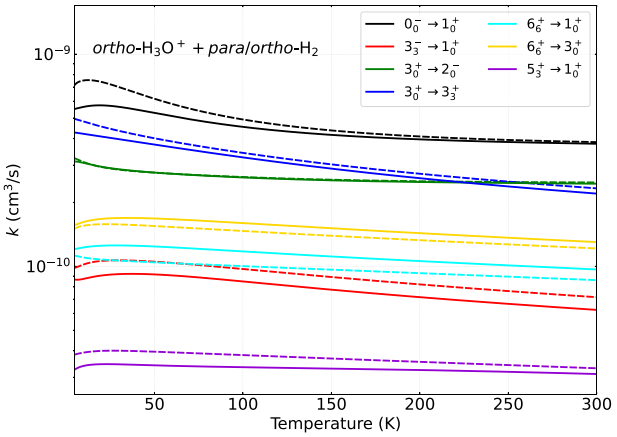

Figure 3. Kinetic temperature dependence of the rate coefficients for the same rotational transitions as shown in Fig. 1 for *o*-H_3O^+ collision with *p*-H_2 (solid lines) and *o*-H_2 (dashed lines) projectiles.

species, while Fig. 2 shows the corresponding cross sections for *p*-H_3O^+ for transitions with randomly selected Δj and Δk parameters and changes in the inversion splitting index.

First, it is important to notice that the cross sections usually monotonically decrease with increasing collision energy (except for some particular transitions) following a typical Langevin behaviour, as expected for ion–molecule collisions (see, for example, the work by Desrousseaux et al. 2019). The few exceptions (see, for example, the $2_1^- \rightarrow 1_1^+$ transition in Fig. 2) are most probably related to wide shape resonances, which are associated with quasi-bound states formed due to the multiple secondary wells along the potential energy surface (see Paper I for PES details). With increasing collision energy (outside the resonances), these cross sections are also expected to follow a Langevin behaviour, at sufficiently high energies, however, they will probably rather flatten. Similar cross sections with wide shape resonances were reported earlier for other multi-well collisional systems, like SH^- – He (Bop et al. 2017), C_5S – He (Khadri, Chefai & Hammami 2020), or HF – He (Stoecklin, Voronin & Rayez 2003). The cross sections are characterized by a very dense resonance structure for all transitions, especially at total energies below 800 – 900 cm $^{-1}$. These Feshbach type and shape (orbiting) resonances are typical for van der Waals type complexes with a large well depth. More rigorously, the Feshbach resonances appear due to the formation of bound states via short trapping of the projectile in the potential well, while the shape resonances are related to quasi-bound states, which are formed due to tunnelling via the centrifugal energy barrier (Costes & Naulin 2016). At higher energies the resonances are not as pronounced, so the energy step size was increased.

Our further important finding following the analysis of cross sections is that the data obtained for the *p*-H_2 and *o*-H_2 projectiles are very similar. This is an expected behaviour, and the same tendency was observed earlier for several other 'ion + molecular hydrogen' collision schemes, for example recently for $NS^+ + H_2$ (Bop, Kalugina & Lique 2022), $HCS^+ + H_2$ (Denis-Alpizar, Quintas-Sánchez & Dawes 2022), HCO^+ and $DCO^+ + H_2$ (Denis-Alpizar et al. 2020), $CF^+ + H_2$ (Desrousseaux et al. 2019), and also for collisions of negative ions like $C_3N^- + H_2$ (Lara-Moreno, Stoecklin & Halvick 2019) or $CN^- + H_2$ (Klos & Lique 2011). According to Lara-Moreno et al. (2019) these similarities between the *p*-H_2 and *o*-H_2 cross sections could be attributed to the features of the short-range interaction of the colliders, which give relevant contributions in the coupling matrix elements equally for *p*-H_2 and *o*-H_2. Also, the long-range part of the PES is weakly anisotropic with respect to the rotation of H_2 (see Paper I for details).

In accordance with the results of previous works, the cross sections we computed with the *ortho*-H_2 projectile are somewhat larger compared to the *para*-H_2 data, but the differences usually do not exceed 10 per cent. It is worth noticing that for some transitions we observe more pronounced differences (up to about 20 – 30 per cent) at higher energies ($\geq$400 cm^{-1}), which is different from what was generally found for other ion + molecule collisions, where the main differences were present in the low-energy regime (see, for example, the works by Bop et al. 2022 and Denis-Alpizar et al. 2022). This feature is most probably associated with the larger anisotropy of the PES with respect to H_2 rotation in the short range. The resonances are not so remarkable in the case of the *o*-H_2 collider (analogously as it was found by other authors), but this feature is likely to be related to the high number of overlapping resonances due to the significantly higher number of channels and couplings compared to *p*-H_2 (remember, the rotational basis involves $j_{H_2} = 0, 2$ for *p*-H_2 and $j_{H_2} = 1, 3$ states for *o*-H_2).

4.2 Rate coefficients

Once the state-to-state cross sections were calculated, we computed the corresponding rate coefficients for the $H_3O^+ - H_2$ collision (see Section 3.2 for details). In Fig. 3, the rate coefficients for the *o*-H_3O^+ collision with both *p*-H_2 and *o*-H_2 colliders are compared for the same rotational transitions which are presented in Fig. 1. In the whole kinetic temperature interval from 10 to 300 K the temperature dependence is relatively weak, which is in accordance with the Langevin capture model. Analogously as in the case of the cross sections, the rate coefficients calculated for *p*-H_2 and *o*-H_2 are very similar both in their behaviour and magnitudes, in agreement with previous findings in the literature (see, for example, Bop et al. 2022, Denis-Alpizar et al. 2022, Desrousseaux et al. 2019, Klos &

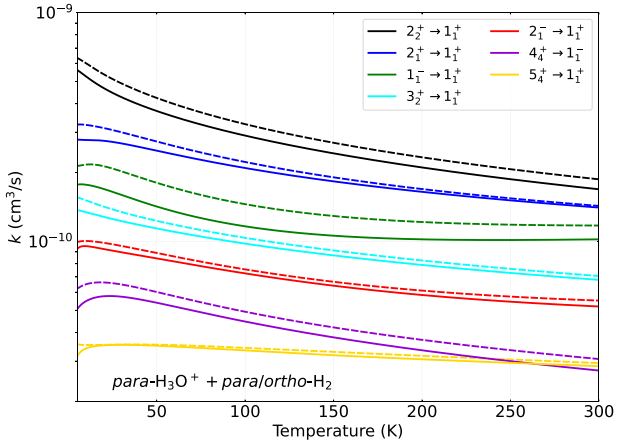

Figure 4. Kinetic temperature dependence of the rate coefficients for the same rotational transitions as shown in Fig. 2 for p-H_3O^+ collision with p-H_2 (solid lines) and o-H_2 (dashed lines) projectiles.

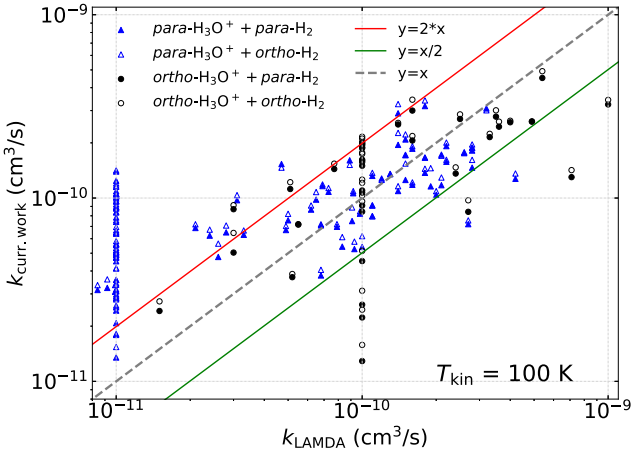

Figure 5. Ratios of our recent state-to-state thermal rate coefficients for all nuclear spin configurations of the $H_3O^+ + H_2$ collision with respect to the corresponding data listed in the LAMDA data base (Schöier et al. 2005) at 100 K kinetic temperature. The reference collisional data in the LAMDA data base are only available for p-H_2 collider.

Lique 2011). The magnitude of the rate coefficients with o-H_2 is somewhat higher for all transitions. These differences are almost constant above 100 K, and usually do not exceed 10 per cent except for some particular transitions for which they can reach a maximum of 15 − 20 per cent.

It is worth noting also that there is no constant linear scaling (uniform temperature dependence) observed between the rate coefficients compared in Fig. 3 with respect to the change in kinetic temperature. If we examine for instance the $0_0^- \rightarrow 1_0^+$ and $3_0^+ \rightarrow 2_0^-$ transitions, we can see some significant differences: for collision with o-H_2 the rate coefficients for the former decrease from 7.5×10^{-9} down to 3.8×10^{-9} cm^3 s^{-1} (i.e. by a factor of 2) between 15 and 300 K, while for the latter transition the rate coefficients are quasi-constant in the whole temperature range. The rate coefficients exhibit a non-linear behaviour on the logarithmic scale dominantly only in the low-temperature regime, i.e. below 50 K. The close magnitude and similar temperature dependence of the state-to-state rate coefficients computed with p-$H_2(j = 0)$ and o-$H_2(j = 1)$ colliders imply a weak dependence of the collisional data on the rotational state of H_2. Based on this one can expect that the rate coefficients for H_3O^+ should be very similar in collision with a rotationally hot hydrogen projectile ($j_{H_2} = 2, 3, ...$).

In Fig. 4, the rate coefficients for the p-H_3O^+ collision with both p-H_2 and o-H_2 nuclear spin isomers are compared again up to 300 K for the same rotational transitions which are presented in Fig. 2. The overall behaviour and the variation of the rate coefficients with temperature are very similar to what was found in the case of the o-H_3O^+ nuclear spin species. The rate coefficients computed with p-H_2 and o-H_2 colliders are similar, the differences between them is similar to those discussed in the paragraph above.

We have compared our rate coefficients with the corresponding data from the LAMDA data base (Schöier et al. 2005, see also van der Tak et al. 2020). Currently these latter are used for astrophysical modelling of hydronium in interstellar clouds, but the data are rather limited: only a single set of rate coefficients are provided for H_3O^+ for 100 K kinetic temperature, and only with the p-H_2 collider. Another important limitation is that the data base involves collisional and spectroscopic data for states with $K \leq 3$ only, missing some important states which can be populated $\geq$100 K. The collisional rate coefficients in the current LAMDA datafile were estimated from scaled radiative rates, following the scaling procedure described by van der Tak et al. (2020). For the non-radiative (dipole-forbidden) transitions, NH_3 collisional data of Danby et al. (1988) were adopted, because NH_3 is isoelectronic with H_3O^+ and the two species are very similar in molecular mass. This places the H_3O^+ LAMDA datafile in the category 'rough scalings / similar species', which has an estimated uncertainty of a factor of 10, according to van der Tak et al. (2020). In contrast to this, we are providing exact rate coefficients for all nuclear spin species (including o-H_2) for a wide range of $T_{\rm kin}$ from 10 up to 300 K.

Due to the mentioned limitations of the reference data, in Fig. 5, we present ratios of the state-to-state rate coefficients with respect to the corresponding data from LAMDA at 100 K, for both o-H_3O^+ and p-H_3O^+. As one can see, the ratios show a large scatter: no linear scaling trends can be observed between our collisional rate coefficients and those from the LAMDA data base. The calculated ratios imply significant differences between the compared sets of rate coefficients, with typical differences of up to a factor of 2 in both directions. Due to the rough scaling, some of the rate coefficients in the LAMDA data base are likely to be overestimated at values of 10^{-10} cm^3 s^{-1}, while on the opposite side, some low-magnitude collisional data are likely underestimated (in particular the series of rate coefficients at 10^{-11} cm^3 s^{-1}). Therefore, it is not surprising that our quantum-level calculations show differences even up to a factor of 10 with the roughly scaled data.

Compared to the large variations with respect to the LAMDA values, no significant differences can be found in Fig. 5 between our data computed with o/p-H_2 colliders. Some slight tendencies could be observed however. For instance, the large-magnitude rate coefficients from LAMDA systematically overestimate our collisional data. For the low-magnitude transitions (with values below about 2×10^{-10} cm^3 s^{-1}) we find an opposite trend however: the LAMDA data are significantly lower than ours. This means that the collisional data, which were used for astrophysical modelling before, overestimated the de-excitation probability of the dominant transition channels, while the contributions from weaker channels were underestimated. All these could lead to large uncertainties in previous modellings, and the improved set of rate coefficients we present here will have a significant impact on the abundance

and excitation modelling of hydronium, especially in warm dense molecular clouds in the ISM.

5 RADIATIVE TRANSFER MODELLING OF HYDRONIUM IN WARM INTERSTELLAR CLOUDS

Radiative transfer modelling was performed to study the excitation of H_3O^+ in astrophysical media based on the new set of rate coefficients with *ortho*- and *para*-H_2 colliders. The calculations were performed using the latest version of the RADEX non-LTE radiative transfer computer program (van der Tak et al. 2007) based on the large velocity gradient (LVG) approximation. The new set of rate coefficients allows one to explore a significantly larger range of kinetic temperatures (up to $T = 300$ K) compared to our previous work (Paper II) and also supports more reliable radiative transfer modelling for these high temperatures due to the new, previously missing collisional data for *o*-H_2, which becomes the dominant collider above 100 K. The *ortho*-to-*para* ratio of H_2 at different temperatures was considered based on an LTE-distribution, as implemented in the RADEX software: 0.23/0.77 at 50 K, 0.62/0.38 at 100 K, 0.75/0.25 at 200 and 300 K. However, due to the similarities between the *o*/*p*-H_2 collisional data, we do not expect significant impact on the modelling with respect to the variation of the *ortho*-to-*para* ratio.

The aim of the radiative transfer modellings performed in this work is to demonstrate the impact of our new rate coefficients on the inferred column densities, and not to re-analyse and re-interpret the previous observations. For this purpose we compare the radiation (brightness) temperatures computed by using two different sets of collisional rate coefficients (similar modelings were performed in Paper II). For the first (reference) set we adopted the available rate coefficients for H_3O^+ from the LAMDA data base (Schöier et al. 2005), which are available only for 100 K and were derived from the scaled $NH_3 - p$-$H_2(j = 0)$ collisional data of Danby et al. (1988), considering also the cross sections reported by Offer & van Hemert (1992). As the second set we have used our new rate coefficients, which cover a much larger temperature range (10–300 K) and all possible nuclear species, including *o*-H_2. The rotational energies along with the frequencies and Einstein *A*-coefficients of the modelled radiative transition were taken from the JPL data base (Pickett, Cohen & Drouin 2010, Species Tag: 19004, version 3, compiled by Yu & Drouin, 2010 January). For more details about the states involved in the calculations, see Table A1 in Appendix A.

As shown in Section 2, H_3O^+ was detected in several environments, which possess very different physical conditions. For example, in diffuse molecular clouds H_2-densities from 35 up to 10^3 cm^{-3} were reported, while for dense clouds the hydrogen densities can be as high as 10^8 cm^{-3}, but are typically around 10^6 cm^{-3}. For column densities the observations report several values in a broad range from 0.7×10^{13} up to 7×10^{16} cm^{-2}. The typical temperatures of the environments, where hydronium was detected, are $\geq$100 K, but some authors reported higher temperatures as well ($\sim$200, $\sim$240, $\sim$380, and even $\sim$500 K). In diffuse ISM sources, H_3O^+ lines are usually detected in absorption (Gerin et al. 2010; Lis et al. 2014; Indriolo et al. 2015). It is worth mentioning however that emission from the $0_0^- \rightarrow 1_0^+$ (984.7 GHz) line is also reported by Indriolo et al. (2015), which confirms the necessity of collisional rate coefficients even for low-density clouds. For this reason, we decided to calculate the radiation temperatures for all observed transitions of H_3O^+ under specific, constrained physical conditions, which were carefully selected based on the reported observations. In particular, 50, 100, 200, and 300 K kinetic temperatures were considered to cover the majority of the observations, but not going beyond the upper limit of our rate coefficients. We separately modelled diffuse and dense cloud conditions with hydrogen densities of 10^3 and 10^6 cm^{-3}, respectively. In terms of column densities we have decided to sample strictly optically thin regions with 1×10^{13} cm^{-2} as well as optically thick clouds with 1×10^{16} cm^{-2}, which nearly cover the lower and upper boundaries of the reported observations. For the modellings in the optically thin region the opacity $\tau \ll 1$, while under optically thick conditions $\tau \simeq 1$–1000 except for some particular transitions at low H_2-density (10^3 cm^{-3}). The background temperature and the line width parameters were kept fixed in the calculations at $T_{\rm bg} = 2.7$ K and $\Delta V = 1.0$ km s^{-1}, respectively.

To demonstrate the reliability of our modellings, in Paper II we have calculated the radiation temperatures at $T_{\rm kin} = 50$ and 100 K for the $1_1^- \rightarrow 2_1^+$, $3_2^+ \rightarrow 2_2^-$, and $3_0^+ \rightarrow 2_0^-$ transitions, which showed a good quantitative agreement with the results of Phillips et al. (1992). In this paper however, we compare the relative ratio of radiation temperatures for the observed radiative transitions of both *ortho*- and *para*-H_3O^+ calculated for diffuse [Fig. 6.(a)] and dense [Fig. 6.(b)] molecular cloud conditions. The $T_{\rm R}^{\rm curr.work}$ radiation temperatures are computed from our new set of rate coefficients, while the $T_{\rm R}^{\rm LAMDA^*}$ set is calculated based on the corresponding collisional data from the LAMDA data base (Schöier et al. 2005). The solid colour bars correspond to radiative transfer calculations in the optically thin environment ($N = 10^{13}$ cm^{-2}), while the hatch-filled colour bars show the same ratios at large column densities ($N = 10^{16}$ cm^{-2}).

As one can see in Fig. 6, there are very significant differences between the radiation temperatures calculated with the two set of rate coefficients. A ratio close to unity is observed only for very few transitions, under specific physical conditions. Also, no coherence patterns were found for the data presented, and the $T_{\rm R}$ ratios depend very strongly both on the kinetic temperature, on the H_3O^+ column and H_2 volume densities as well as on the particular rotational transitions. There are some slight trends towards temperature dependence only, since the ratios are usually decreasing as $T_{\rm kin}$ increases. Even this is not a strict rule however and several deviations from this are observed, most notably for larger column densities (i.e. for 10^{16} cm^{-2}). Moreover, since this tendency is mostly valid for the $T_{\rm R}$ ratios much below unity as well, we can observe the highest relative deviations at higher $T_{\rm kin}$. In particular, the radiation temperature ratio can be as low as $\sim$0.02 for the $4_0^- \rightarrow 3_0^+$ transition at 4232 GHz in Fig. 6.(b), which means that the $T_{\rm R}$ calculated for this line with our new set of rate coefficients is more than a factor of 50 smaller than that is calculated from the LAMDA data. On the other hand, for the very close $4_1^- \rightarrow 3_1^+$ *para*-H_3O^+ transition at 4241 GHz an opposite tendency is observed: at 50 and 100 K differences up to more than a factor of 7 are found in the other direction. For most transitions the $T_{\rm R}$ ratios vary between 0.5 and 2. Larger than a factor of 3 differences are found for the $4_1^- \rightarrow 3_1^+$ and $4_2^- \rightarrow 3_2^+$ transitions most notably, as well as for some other transitions at 300 K (see the 307 and 396 GHz lines at 10^3 cm^{-3} and the 2981 and 4232 GHz lines at 10^6 cm^{-3} gas density). The observed large variation of the ratios are not only associated with the differences in the magnitude of the corresponding rate coefficients, but also to the larger temperature range covered, larger number of rotational states involved as well as to the presence of collisional data with *ortho*-H_2 collider presented in this work (although its impact is limited to $\sim$ 20 per cent). These conclusions are supported also by the fact that large differences are found also for radiation temperatures, which are calculated close to LTE conditions (with $n(H_2) = 10^6$ cm^{-3}), where the state-to-state collisional rate coefficients usually have less

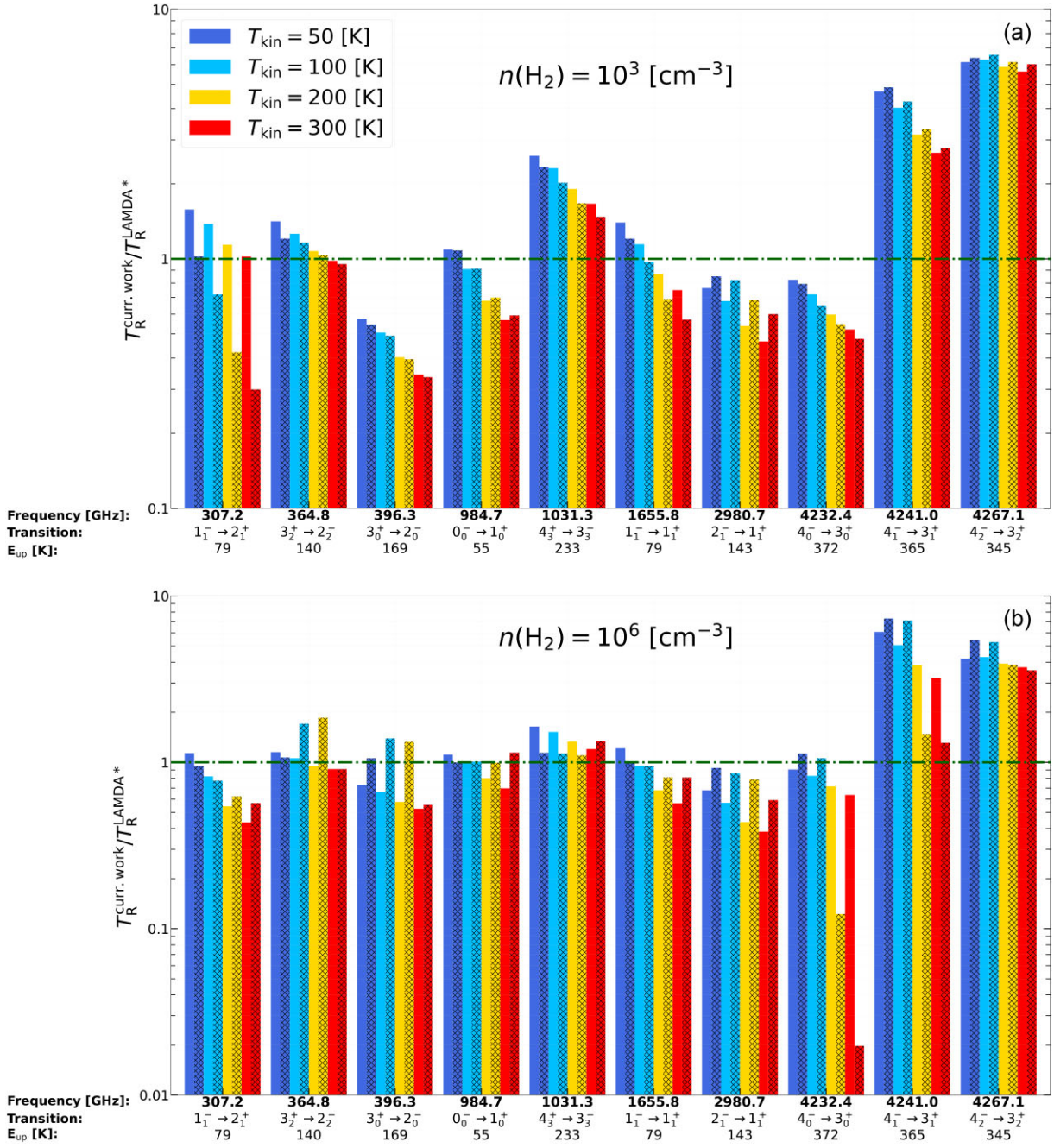

Figure 6. The relative ratio of radiation temperatures at 50, 100, 200, and 300 K kinetic temperatures for the majority of the observed radiative H_3O^+ transitions calculated for diffuse [panel (a), $n(H_2) = 10^3$ cm^{-3}] and dense [panel (b), $n(H_2) = 10^6$ cm^{-3}] molecular cloud conditions. The $T_R^{curr.work}$ data is computed from our new set of rate coefficients, while the $T_R^{LAMDA^*}$ set is calculated based on the corresponding collisional data from the LAMDA data base (Schöier et al. 2005). The colour bars correspond for radiative transfer calculations in the optically thin environments ($N = 10^{13}$ cm^{-2}), while the hatch-filled bars show the same quantities, but for optically thick regions ($N = 10^{16}$ cm^{-2}).

influence on the results of radiative transfer modellings. About the rotational states involved it is important to mention that we have considered 21 *para*- and 11 *ortho*-H_3O^+ levels, including states with $K \leq 6$ quantum numbers, while the LAMDA data base provides rate coefficients for 14 and 9 levels of them, respectively, with $K \leq 3$ only. In addition to the higher rotational states (i.e. those with $j = 5$), the LAMDA set of rate coefficients also excludes some of the lower states (see Table A1 in Appendix A for details), which can be populated already at moderate temperatures (from about 100 K). Due to this, some of the rotational levels could be overpopulated in radiative transfer modelling, which can lead to additional significant differences when using the LAMDA rate coefficients or those from this work. To estimate the magnitude of these differences, we have also computed the T_R ratios with an equivalent set of rotational states, thus involving our present rate coefficients only for those levels, which are present in the LAMDA data base, and neglecting all others in the radiative transfer model. We found that the ratios of the radiation temperatures still significantly deviate from unity, which confirms

that the largest impact is related to the differences in magnitude of the rate coefficients. The other, non-negligible, contribution is due to the missing levels and transitions. It is also important to notice that population inversion can be observed for several transitions of hydronium under non-LTE conditions, and the new collisional data have a significant impact of their characteristics even at lower kinetic temperatures, as we demonstrated earlier in Paper II for some low-frequency transitions at 50 and 100 K (see Section 3.3 therein).

In general, Fig. 6.(a) and (b) show that the variation of the $T_R^{\rm curr.work}/T_R^{\rm LAMDA^*}$ relative ratios are large and not clearly correlated to any physical properties. The ratios are changing notably from transition to transition and there are no unambiguous patterns of their dependence on the particular upper or lower rotational states. There is no correlation found neither with respect to molecular, neither column densities. The only systematic behaviour found is the slight kinetic temperature dependence, which is also not valid for all transitions and at any density conditions. Based on these findings we conclude that the new rate coefficients proposed in this work have a significant impact on astrophysical modellings, more particularly on the determination of column densities. This can lead consequently to more precise interpretation of H_3O^+ observations in various dense and diffuse interstellar environments by deriving more accurate hydronium abundances, which can be remarkably different from those reported previously for this species.

6 CONCLUSIONS

We have presented in this work state-to-state rotational de-excitation cross sections and thermal rate coefficients for the collision of hydronium (H_3O^+) with molecular hydrogen. For theoretical calculations the best available and most accurate close-coupling scattering theory has been used based on our state-of-the-art five-dimensional rigid-rotor potential energy surface (Paper I). All nuclear spin configurations (*ortho/para*) are considered for both colliding partners, so the collisions with *ortho*-H_2 were studied as well, which is the most abundant collider in interstellar clouds with temperatures above 100 K.

As it is expected to be valid for all 'ion + molecule' collisional systems, most of the cross sections monotonically decrease as the collision energy is increasing, following a typical Langevin behaviour. They exhibit a very dense resonance behaviour, especially below 800 – 900 cm^{-1} kinetic energies, which are associated with the formation of bound and quasi-bound states in the potential well. We have also found that there are no significant differences between the collisional data computed with *ortho*- and *para*-H_2 colliders. Due to this, one can expect that H_3O^+ collisional data are similar for collisions with rotationally hot hydrogen $H_2(j \geq 2)$. We have observed also a relatively weak temperature dependence in the case of the rate coefficients.

Having a full set of collisional data for all rotational levels of hydronium below 430 K ($\sim$300 cm^{-1}), we have presented a comparison for all particular rotational transitions individually with the available rate coefficients from the LAMDA data base (Schöier et al. 2005), which were used earlier by many authors for the interpretation of H_3O^+ observations in interstellar clouds. Significant differences are found between the two data sets, typically up to a factor of 2, but occasionally up to a factor of 10. The tendencies we observed in this analysis indicate that the collisional data, which were used earlier for astrophysical modelling, overestimate the de-excitation probability of the dominant channels, while the weaker channels are underestimated.

In order to examine the impact of the new rate coefficients on the astrophysical models, we have performed radiative transfer modelling of H_3O^+ based on the LVG approximation by the RADEX non-LTE code. We compare the radiation temperatures computed by using two sets of rate coefficients: first, the available data for H_3O^+ from the LAMDA data base (Schöier et al. 2005) and, second, the new collisional rate coefficients presented in this work. We observed very significant differences between the T_R calculated with the two set of rate coefficients, once we compared their relative ratios. For most of the lines the ratios of the calculated radiation temperatures are far from unity, typically within factors of 2 in either direction, which is similar to what was found for the rate coefficients. They also depend very strongly on the kinetic temperature, column, and hydrogen densities as well as on the particular transitions, so they do not correlate with the physical conditions. It is important to notice that these large variations of the ratios are not only associated with the differences between the state-to-state rate coefficients, but also with the larger temperature range covered, the larger number of rotational levels involved as well as to the additional collisional data for *ortho*-H_2.

Based on the results of the analysis in this work we conclude that the new, accurate (within 25 – 30 per cent) rate coefficients without doubt have a significant impact on the radiative transfer modelling of astronomical environments, including dense and diffuse molecular clouds. Consequently, the new collisional data allow a more adequate interpretation of hydronium observations in interstellar clouds, leading to more accurate estimations for column densities and relative abundances of hydronium, especially in warmer molecular clouds of the ISM at $T \geq 100$ K. This ensures a more robust indirect way to estimate the rate of O_2 and H_2O production in interstellar regions.

ACKNOWLEDGEMENTS

We acknowledge financial support from the European Research Council (Consolidator Grant COLLEXISM, Grant Agreement No. 811363) and the Programme National 'Physique et Chimie du Milieu Interstellaire' (PCMI) of CNRS/INSU (Centre National de la Recherche Scientifique/Institut National des Sciences de l'Univers) with INC/INP (Institut de Chimie/Institut de Physique) cofunded by CEA (Commissariat à l'Energie Atomique et aux Energies Alternatives) and CNES (Centre National d'Etudes Spatiales). We wish to acknowledge the support from the CEA/GENCI (Grand Équipement National de Calcul Intensif) for awarding us access to the TGCC (Très Grand Centre de Calcul) Joliot Curie/IRENE supercomputer within the A0110413001 project and also the KIFÜ (Kormányzati Informatikai Fejlesztési Ügynökség) for awarding us access to HPC (High-Performance Computing) resources based in Hungary. SD acknowledges the support from COST Action CA18212 - Molecular Dynamics in the GAS phase (MD-GAS), supported by COST (European Cooperation in Science and Technology). FL acknowledges the Institut Universitaire de France.

The authors dedicate this paper to the memory of Tom Phillips, a pioneer of submillimeter observations in general and astronomical H_3O^+ spectroscopy in particular, who passed away on August 6, 2022, at the age of 85.

DATA AVAILABILITY

The data that support the findings of this study are available within the article and its supplementary material at MNRAS online.

The molecular data files in RADEX-format, which were used in the radiative transfer calculations, and which include the particular

state-to-state rate coefficients for *ortho/para*-H_3O^+ collisions with *ortho/para*-H_2 up to 300 K are provided as supplementary material. The data files containing the energy-dependent de-excitation cross sections are also provided as supplementary material.

The data underlying this article will be made publicly available also through the EMAA https://emaa.osug.fr/, LAMDA https://home.strw.leidenuniv.nl/~moldata/, and BASECOL https://basecol.vamdc.eu/ data bases.

REFERENCES

Alexander M. H., Manolopoulos D. E., 1987, J. Chem. Phys., 86, 2044
Ando R. et al., 2017, ApJ, 849, 81
Benz A. O. et al., 2010, A&A, 521, L35
Benz A. O. et al., 2016, A&A, 590, A105
Bop C. T., Trabelsi T., Hammami K., Mogren Al Mogren M., Lique F., Hochlaf M., 2017, J. Chem. Phys., 147, 124301
Bop C. T., Kalugina Y., Lique F., 2022, J. Chem. Phys., 156, 204311
Bouhafs N., Rist C., Daniel F., Dumouchel F., Lique F., Wiesenfeld L., Faure A., 2017, MNRAS, 470, 2204
Bubin S., Adamowicz L., 2003, J. Chem. Phys., 118, 3079
Costes M., Naulin C., 2016, Chem. Sci., 7, 2462
Danby G., Flower D. R., Valiron P., Schilke P., Walmsley C. M., 1988, MNRAS, 235, 229
Demes S., Lique F., Faure A., Rist C., 2020, J. Chem. Phys., 153, 094301 Paper I
Demes S., Lique F., Faure A., van der Tak F. F. S., Rist C., Hily-Blant P., 2021, MNRAS, 509, 1252 Paper II
Denis-Alpizar O., Stoecklin T., Dutrey A., Guilloteau S., 2020, MNRAS, 497, 4276
Denis-Alpizar O., Quintas-Sánchez E., Dawes R., 2022, MNRAS, 512, 5546
Desrousseaux B., Quintas-Sánchez E., Dawes R., Lique F., 2019, J. Phys. Chem. A, 123, 9637
El Hanini H., Najar F., Naouai M., Jaidane N. E., 2019, Phys. Chem. Chem. Phys., 21, 11705
Faure A., Tennyson J., 2003, MNRAS, 340, 468
Faure A., Lique F., Wiesenfeld L., 2016, MNRAS, 460, 2103
Faure A., Hily-Blant P., Rist C., Pineau des Forêts G., Matthews A., Flower D. R., 2019, MNRAS, 487, 3392
Gerin M. et al., 2010, A&A, 518, 1
Godard Palluet A., Thibault F., Lique F., 2022, J. Chem. Phys., 156, 104303
Goicoechea J. R., Cernicharo J., 2001, ApJ, 554, L213
González-Alfonso E. et al., 2013, A&A, 550, A25
Herbst E., Klemperer W., 1973, ApJ, 185, 505
Holdship J. et al., 2022, ApJ, 931, 89
Hollenbach D., Kaufman M. J., Neufeld D., Wolfire M., Goicoechea J. R., 2012, ApJ, 754, 105
Hollis J. M., Churchwell E. B., Herbst E., De Lucia F. C., 1986, Nature, 322, 524
Indriolo N. et al., 2015, ApJ, 800, 40
Jensen M. J., Bilodeau R. C., Safvan C. P., Seiersen K., Andersen L. H., Pedersen H. B., Heber O., 2000, ApJ, 543, 764
Khadri F., Chefai A., Hammami K., 2020, MNRAS, 498, 5159
Klos J., Lique F., 2011, MNRAS, 418, 271
Lara-Moreno M., Stoecklin T., Halvick P., 2019, MNRAS, 486, 414
Lis D. C. et al., 2014, ApJ, 785, 135
Manolopoulos D. E., 1986, J. Chem. Phys., 85, 6425
Martín S. et al., 2021, A&A, 656, A46
Offer A. R., van Hemert M. C., 1992, Chem. Phys., 163, 83
Phillips T. G., van Dishoeck E. F., Keene J., 1992, ApJ, 399, 533
Pickett H. M., Cohen E. A., Drouin B. J., 2010, J. Quant. Spectrosc. Radiat. Transfer, 111, 1617
Pirlot P., Kalugina Y. N., Ramachandran R., Raffy G., Dagdigian P. J., Lique F., 2021, J. Chem. Phys., 155, 134303
Rist C., Alexander M. H., Valiron P., 1993, J. Chem. Phys., 98, 4662
Roueff E., Lique F., 2013, Chem. Rev., 113, 8906
Schöier F. L., Van Der Tak F. F., Van Dishoeck E. F., Black J. H., 2005, A&A, 432, 369
Sternberg A., Dalgarno A., 1995, ApJS, 99, 565
Stoecklin T., Voronin A., Rayez J., 2003, Chem. Phys., 294, 117
Tang J., Oka T., 1999, J. Mol. Spectrosc., 196, 120
Timmermann R., Nikola T., Poglitsch A., Geis N., Stacey G. J., Townes C. H., 1996, ApJ, 463, L109
Valiron P., Wernli M., Faure A., Wiesenfeld L., Rist C., Kedžuch S., Noga J., 2008, J. Chem. Phys., 129, 134306
van der Tak F. F. S., Black J. H., Schöier F. L., Jansen D. J., van Dishoeck E. F., 2007, A&A, 468, 627
van Dishoeck E. F., Herbst E., Neufeld D. A., 2013, Chem. Rev., 113, 9043
van der Tak F. F. S., Belloche A., Schilke P., Güsten R., Philipp S., Comito C., Bergman P., Nyman L.-A., 2006, A&A, 454, L99
van der Tak F. F. S., Aalto S., Meijerink R., 2008, A&A, 477, L5
van der Tak F. F. S., Müller H. S. P., Harding M. E., Gauss J., 2009, A&A, 507, 347
van der Tak F. F. A. W., Liu L., Güsten R., 2016, A&A, 593, A43
van der Tak F. F. S., Lique F., Faure A., Black J. H., van Dishoeck E. F., 2020, Atoms, 8, 15
Wootten A., Boulanger F., Bogey M., Combes F., Encrenaz P. J., Gerin M., Ziurys L., 1986, A&A, 166, L15
Wootten A., Mangum J. G., Turner B. E., Bogey M., Boulanger F., Combes F., Encrenaz P. J., Gerin M., 1991, ApJ, 380, L79
Yu S., Drouin B. J., Pearson J. C., Pickett H. M., 2009, ApJS, 180, 119

SUPPORTING INFORMATION

Supplementary data are available at *MNRAS* online.
Please note: Oxford University Press is not responsible for the content or functionality of any supporting materials supplied by the authors. Any queries (other than missing material) should be directed to the corresponding author for the article.

APPENDIX A: A NOTE ON THE ROTATIONAL LEVELS OF H_3O^+ CONSIDERED IN THE SCATTERING CALCULATIONS

The complete set of the rotational states j_k^ϵ considered in this work both for *ortho*- and *para*-H_3O^+ are provided in Table A1 (j is the total angular momentum of the H_3O^+ cation, k is its projection on the C_3 rotational axis, and $\epsilon = \pm$ is an inversion symmetry index). *Ortho*-H_3O^+ is characterized with $k = 3n$ quantum numbers (where $n = 0, 1, 2, \ldots$), while all other k quantum numbers (e.g. $k = 1, 2, 4, 5, \ldots$) refer to *para*-H_3O^+. For *ortho*-H_2 and *para*-H_2 the two lowest rotational states were taken into account in the scattering calculations, i.e. $j_{H_2} = 0, 2$ and $j_{H_2} = 1, 3$, respectively.

Table A1. List of the rotational energy levels (in cm^{-1} and K) of *ortho*- and *para*-H_3O^+, which were considered in collisional studies of this work. The corresponding energies are taken from the JPL data base (Pickett et al. 2010, Species Tag: 19004, version 3, compiled by Yu & Drouin, 2010 January). The state labels with star (∗) symbol indicate those H_3O^+ levels, which are missing in the LAMDA data base (Schöier et al. 2005).

	para-H_3O^+				*ortho*-H_3O^+		
state label	rotational state j_k^ϵ	rotational energy [cm^{-1}]	[K]	state label	rotational state j_k^ϵ	rotational energy [cm^{-1}]	[K]
(1)	1_1^+	0.000	0.0	(1)	1_0^+	5.101	7.3
(2)	2_2^+	29.697	42.4	(2)	0_0^-	37.947	54.2
(3)	2_1^+	44.986	64.3	(3)	3_3^+	71.681	102.4
(4)	1_1^-	55.233	78.9	(4)	2_0^-	104.239	148.9
(5)	2_2^-	84.977	121.4	(5)	3_0^+	117.457	167.8
(6)	3_2^+	97.145	138.8	(6)	3_3^-	127.172	181.7
(7)	2_1^-	99.427	142.1	(7)	4_3^+	161.573	230.9
(8)	3_1^+	112.384	160.6	(8)	4_3^-	215.486	307.9
(9)∗	4_4^+	125.939	179.9	(9)	4_0^-	258.636	369.5
(10)	3_2^-	151.241	216.1	(10)∗	6_6^+	271.201	387.5
(11)	3_1^-	165.657	236.7	(11)∗	5_3^+	273.697	391.1
(12)∗	4_4^-	181.807	259.8				
(13)	4_2^+	186.926	267.1				
(14)∗	5_5^+	192.453	275.0				
(15)	4_1^+	202.099	288.8				
(16)∗	5_4^+	238.256	340.4				
(17)	4_2^-	239.479	342.2				
(18)∗	5_5^-	248.863	355.6				
(19)	4_1^-	253.850	362.7				
(20)∗	5_4^-	292.146	417.4				
(21)∗	5_2^+	298.914	427.1				

APPENDIX B: A NOTE ON THE CONVERGED VALUES OF THE BASIS SET SIZE, ENERGY STEP SIZE AND TOTAL ANGULAR MOMENTA IN SCATTERING CALCULATIONS

The values of the j_{max}, J_{tot}, and E_{step} parameters are discussed here for all total energy intervals ranging from E_{init} to E_{fin}. These particular parameters are used in inputs for our close-coupling scattering calculations and their values were selected following systematic convergence test calculations with a maximum of 1 per cent mean deviation threshold criteria for j_{max} and 0.01 per cent for J_{tot}, respectively. Table B1 shows the corresponding parameters for *ortho*-H_3O^+ and *para*-H_3O^+ collision with *para*-H_2, while Table B2 provides those for collision with *ortho*-H_2 projectile. Due to the higher ground rotational level of *ortho*-H_2, the maximum total energy considered for collision with this species is consequently higher.

Table B1. The converged values of rotational basis size (j_{max}) and maximum total angular momentum (J_{tot}) parameters for the particular total energy intervals (from E_{init} to E_{fin}) for the *o/p*-H_3O^+ – *p*-H_2 collision. The step size for the energies (E_{step}) in these intervals are also listed.

ortho-H_3O^+ − *para*-H_2 collision					*para*-H_3O^+ − *para*-H_2 collision				
E_{init} [cm^{-1}]	E_{fin} [cm^{-1}]	E_{step} [cm^{-1}]	j_{max}	J_{tot}	E_{init} [cm^{-1}]	E_{fin} [cm^{-1}]	E_{step} [cm^{-1}]	j_{max}	J_{tot}
55.4	99.9	0.1	9	23	47.1	74.9	0.1	17	18
100	149.9	0.1	9	30	75	99.9	0.1	17	22
150	174.5	0.5	9	34	100	124.9	0.1	17	26
175	199.5	0.5	9	35	125	149.9	0.1	17	30
200	224.5	0.5	10	42	150	174.5	0.5	17	34
225	249.5	0.5	10	43	175	199.5	0.5	17	38
250	349.5	0.5	10	50	200	224	1	17	39
350	374.5	0.5	10	51	225	249	1	17	43
375	399.5	0.5	10	55	250	274	1	17	44
400	424.5	0.5	10	56	275	299	1	17	48
425	449.5	0.5	12	57	300	324	1	17	49
450	474.5	0.5	12	58	325	374	1	17	51
475	499.5	0.5	12	60	375	399	1	17	52
500	508	2	12	73	400	424	1	17	53
510	522.5	2.5	12	73	425	449	1	17	54
525	547.5	2.5	12	74	450	474	1	17	55
550	570	5	12	74	475	499	1	17	56
575	620	5	12	79	500	518.75	1.25	17	58
625	645	5	12	81	520	547.5	2.5	17	58
650	670	5	12	82	550	570	5	17	59
675	695	5	12	83	575	620	5	17	60
700	720	5	13	84	625	695	5	16	62
725	745	5	13	85	700	745	5	16	63
750	770	5	13	87	750	800	5	16	65
775	800	5	13	93	810	820	10	16	66
810	900	10	13	94	830	870	10	16	68
910	950	10	13	95	880	920	10	15	70
960	980	20	13	95	930	940	10	15	71
1000	–	50	13	98	950	970	10	15	71
1050	–	50	13	106	980	990	10	14	72
1100	1150	50	13	107	1000	1020	20	14	73
1200	1250	50	13	109	1040	–	20	14	75
1300	1350	50	13	112	1060	1080	20	14	77
1400	–	50	13	120	1100	–	50	14	78
1450	1500	50	13	121	1150	–	50	13	78
					1200	–	50	13	80
					1250	–	50	13	84
					1300	–	50	13	89
					1350	–	50	13	91
					1400	–	50	13	93
					1400	1500	50	13	94

Table B2. The converged values of rotational basis size (j_{max}) and maximum total angular momentum (J_{tot}) parameters for the particular total energy intervals (from E_{init} to E_{fin}) for the *o/p*-H_3O^+ – *o*-H_2 collision. The step size for the energies (E_{step}) in these intervals are also listed.

ortho-H_3O^+ − *ortho*-H_2 collision					*para*-H_3O^+ − *ortho*-H_2 collision				
E_{init} [cm^{-1}]	E_{fin} [cm^{-1}]	E_{step} [cm^{-1}]	j_{max}	J_{tot}	E_{init} [cm^{-1}]	E_{fin} [cm^{-1}]	E_{step} [cm^{-1}]	j_{max}	J_{tot}
175.0	199.9	0.1	16	26	165.9	174.9	0.1	16	22
200.0	224.9	0.1	16	27	175.0	199.9	0.1	16	29
225.0	249.9	0.1	17	31	200.0	249.9	0.1	16	36
250.0	274.9	0.1	17	35	250.0	274.9	0.1	16	38
275.0	299.9	0.1	16	42	275.0	299.9	0.1	16	45
300.0	320.0	0.2	16	46	300.0	319.8	0.2	16	52
320.5	324.5	0.5	16	46	320.5	349.5	0.5	16	56
325.0	374.8	0.5	16	67	350.0	500.0	0.5	16	60
375.0	499.5	0.5	18	67	502.5	547.5	2.5	16	60
500.0	520.0	1	18	67	550.0	597.5	2.5	17	64
522.5	-	2.5	18	67	600.0	647.5	2.5	17	68
525.0	547.5	2.5	16	67	650.0	697.5	2.5	17	75
550.0	597.9	2.5	16	69	705	820	5	16	75
600.0	647.5	2.5	16	71	825	870	5	16	77
650.0	674.5	2.5	16	72	875	920	5	16	80
675.0	697.5	2.5	16	73	925	945	5	14	80
700	795	5	16	74	950	995	5	14	87
800	845	5	16	75	1000	1090	10	14	89
850	895	5	15	78	1100	1120	10	14	90
900	995	5	15	88	1130	1140	10	13	91
1000	1120	10	14	88	1150	1200	10	13	96
1130	1170	10	14	89	1220	1260	20	13	96
1180	1240	10	13	91	1280	1320	20	13	103
1250	1270	10	13	101	1340	–	20	12	103
1280	1290	10	12	103	1360	1400	20	12	106
1300	1350	50	12	103	1450	1500	50	12	106
1400	1400	50	11	103	1550	1650	50	12	117
1500	-	50	11	109	1700	–	50	12	122
1600	1700	50	11	110					

This paper has been typeset from a TEX/LATEX file prepared by the author.